Supporting information

Facile ZIF–8 nanocrystals interlayered solvent–resistant thin–film nanocomposite membranes for enhanced solvent permeance and rejection

Yayu Wei[1], Zhe Yang[2], Ling Wang[1], Yifei Yu[1], Hong Yang[1], Hua Jin[1], Peng Lu[1,4]*, Yi Wang[3]*, Dapeng Wu[1], Yanshuo Li[1]*, Chuyang Y. Tang[2]

[1] School of Materials Science and Chemical Engineering, Ningbo University, 818 Fenghua Road, Ningbo, 315211, P. R. China

[2] Department of Civil Engineering, the University of Hong Kong, Hong Kong, SAR 999077, P. R. China

[3] State Key Lab of NBC Protection for Civilian, Beijing, 102205, P. R. China

[4] State Key Laboratory of Fine Chemicals, Dalian University of Technology, Dalian, 116000, P. R. China

*Corresponding author:

Prof. Peng Lu, and Prof. Yanshuo Li,

School of Materials Science and Chemical Engineering, Ningbo University, 818 Fenghua Road, Ningbo, 315211, P. R. China

E-mail: lupeng@nbu.edu.cn; liyanshuo@nbu.edu.cn

Prof. Yi Wang,

State Key Lab of NBC Protection for Civilian, Beijing, 102205, P. R. China

E-mail: wangyi102205@sina.com

Abstract

Introduction of nanomaterials into thin–film nanocomposite (TFN) membranes can improve the solvent permeance for organic solvent reverse (OSRO) and forward osmosis (OSFO) processes. However, the severe nanomaterials aggregation and the formation of defects in membrane rejection layer, which decreased the rejection of membrane against various solutes. Herein, we proposed a novel strategy of thin–film nanocomposite (TFNi) membrane featuring an interlayer of metal–organic framework (MOF, ZIF–8) by one–step fabrication in the simultaneous phase–inversion and crosslinking process. This strategy integrates the precipitation of polyimide (PI) substrates, crosslinking between the PI and hexanediamine, and generated ZIF–8 nanocrystals through the interfacial diffusion. Furthermore, one–step strategy of ZIF–8 effectively mitigate its agglomeration in the surface of support layers by SEM characterization. A prepared polyamide (PA) rejection layer with high crosslinking and low thickness was characterized by XPS and TEM. The resulting TFNi membranes with ZIF–8 interlayer (OSFO$_{ISG}$–2.5) showed a molecular weight cut–off of ~500 Da, the remarkable DI water and THF permeances (9.73 and 1.62 L m^{-2} h^{-1} bar^{-1} under RO mode), and the higher ethanol fluxes (2.10 ± 0.11 LMH under FO mode and 2.97 ± 0.31 LMH under PRO mode). In addition, the solvents permeance of the OSFO$_{ISG}$–2.5 membrane was furtherly improved by 10 h DMF activation without loss of the polystyrene rejection in RO mode. This study also provides insight for the preparation of ZIF–8 on the polymer's matrix for large–scale production.

Keywords: Facile ZIF–8 interlayer, thin–film nanocomposite membrane with an interlayer, simultaneous phase–inversion and crosslinking, high water and solvents permeance.

Introduction

Organic solvents are widely employed in chemosynthesis processes. It is important to develop green and high–efficiency strategies to recycle organic solvents instead of incineration for sustainable development [1]. Conventional solvent recovery processes such as distillation and evaporation suffer from high energy consumption, large carbon footprints, and/or potential environmental impacts [2]. Organic solvent forward osmosis (OSFO), an emerging membrane–based process for solvent filtration, was proposed by Lively and Sholl [3] and demonstrated by Chung and co–workers [4]. OSFO is a promising method for treat the highly concentrated and sensitive solutes, e.g., pharmaceutical ingredients, while offering low fouling tendency. The most important component for OSFO is solvent–resistant OSFO membranes with both high permeance and selectivity.

The incorporation of functional nanomaterials into thin–film composite (TFC) membranes offers a great opportunity to improve their performance [5, 6]. Various nanomaterials, such as zeolite nanoparticles [7], carbon–based nanomaterials (e.g., carbon nanotube [8-10], graphene oxide [11-13], and fullerene [14]), metal oxide nanoparticles (e.g., TiO_2 [15] and SiO_2 [16]), and clay nanosheets (e.g., montmorillonite [17] and layered double hydroxides [18-21]) can be incorporated into polyamide (PA) rejection layers and/or support layers. The resulted thin film composite (TFN) membranes often show significant enhancement in water permeance (e.g., up to 50 – 200%) [22]. Nevertheless, conventional TFN membranes face a challenge, i.e., the trade–off between permeability and selectivity [23], which is often caused by the compromised integrity of PA rejection layers as a result of the aggregation of nanomaterials [24].

Recently, a novel concept of interlayered thin–film nanocomposite membranes (TFNi) was proposed, which involves the pre–loading of a uniform interlayer of nanomaterials on the support layer before forming the PA layer [22]. For example, Livingston and co–workers [25] utilized a sacrificial interlayer of cadmium hydroxide nanostrands for controlling the rate of interfacial polymerization reaction, and the resulting membrane with a sub–10 nm PA layer showed two orders of magnitude higher water flux than that of commercial membranes. Unlike conventional TFN membranes, TFNi membranes with an interlayered structure often show simultaneous enhancement in membrane permeance and permselectivity. The interlayer of TFNi membranes can optimize transport pathways [26, 27] and improve interfacial polymerization reaction [28] (which forms thinner and/or more integral PA layer [25, 29]).

The nanomaterials used for the interlayer of TFNi membranes should be carefully chosen. Metal–organic frameworks (MOFs) as a series of intriguing porous nanomaterials have attracted much research interest in recent years [30-32]. Current approaches of MOF interlayer preparation that have been reported include dip–coating [33], vacuum filtration [11], layer by layer self–assembly [34], and secondary growth [35]. However, the main limitation in these works is that the interfacial compatibility between the MOF and support layers due to their poor adhesion [36]. To improve the interaction between the MOF and support layers of TFNi membranes, *in–situ* growth of MOF nanocrystals in the preformed polymer membranes was proposed to minimize the issue of interfacial compatibility [37-39]. Unfortunately, the reported *in–situ* growth of the MOF process involves multiple steps and could be difficult to scale up [40].

In this work, a novel *in–situ* growth (ISG) strategy of zeolitic–imidazolate framework (ZIF,

ZIF–8) as the interlayer of TFNi membranes in the simultaneous phase–inversion and crosslinking (SIM) process was proposed. To the best of our knowledge, this is the first report on the prepared ZIF–8/PI composite membranes using the SIM process for solvent–resistant support layers. The ZIF as a subclass of MOF has been gaining momentum in membrane materials, due to their ultra–microporous aperture and excellent chemical/hydrothermal stability [41, 42]. Based on our previous work [43], the modified SIM process could effectively reduce the preparation process of solvent–resistant polyimide (PI) support layers. The crosslinked PI membranes combine the amide and imide bonds in the polymer chains [44], which has the natural property of bonding with Zn^{2+} for the nucleation and anchoring of ZIF–8 [45-48]. In addition, the novel ISG strategy not only effectively mitigates the agglomeration of ZIF–8 as the interlayer, but also provides the significant improvement in the solvent permeance of TFNi membranes.

2. Experimental

2.1 Materials

Polyimide (PI) was purchased from Ensinger Sintimid GmbH (TECAPOWDER P84). Commercial polyester nonwoven fabrics (PET grade 3249) was obtained from Ahlstrom, Helsinki, Finland. Polyethylene glycol (PEG) 400 (~99.5%), 1–methyl–2–pyrrolidinone (NMP, anhydrous, ~99.5%), ethanol (EtOH, ~99.5%), isopropyl alcohol (IPA, ~99.5%) and N,N–di–methylformamide (DMF, anhydrous, ~99.8%) were provided by Sinopharm Chemical Reagent Co., Ltd. 1,3–phenylenediamine (MPD, >99%), 1,3,5–benzenetricarbonyl trichloride (TMC, ~98%), and hexanediamine (HDA, >99%) were provided by TCI Chemicals Ltd. A nonpolar organic solvent, Isopar–G (Univar, Redmond, WA) was used to disperse TMC for interfacial polymerization reaction. Lithium chloride (LiCl, 42.39 g mol^{-1}, ≥99%) was provided by Shanghai Titan Technology Co., Ltd. Polystyrene ($[CH_2CH(C_6H_5)]_n$, PS, analytical standard) with different molecular weight were purchased from Sigma–Aldrich (M_w ~500, M_w ~800, and M_w ~1000) and American Polymer Standards (M_w ~200, M_w ~400, and M_w ~1200) Co., Ltd., respectively. Zinc nitrate hexahydrate ($Zn(NO_3)_2{\bullet}6H_2O$) and 2–methylimidazole (Hmim, ~99.5%) were purchased from Shanghai Aladdin Biochemical Technology Co., Ltd. Milli–Q ultrapure water purification system (Millipore, Billerica, MA) was used to produce the Deionized (DI) water.

2.2 Fabrication of solvent–resistant TFNi membranes with ZIF–8 interlayer

2.2.1 Preparation of solvent–resistant PI support layers with ZIF–8 nanocrystals

The novel ISG strategy of ZIF–8 nanocrystals in the solvent–resistant PI support layers' formation process by the modified SIM method are shown in Fig. 1(a). This strategy consisted the phase–inversion of PI support layer, the crosslinking of PI polymer, and the nucleation of ZIF–8 nanocrystals. The key parameters of casting solutions during the modified SIM process were shown in Table 1. The casting solutions contained the PI polymer, NMP solvent, PEG400 pore–forming agent, and a certain amount of $Zn(NO_3)_2{\bullet}6H_2O$. The casting solutions were stirred at room temperature for 12 h to form homogeneous solutions and then degassed for 8 h to remove the bubbles before the casting. Next, the casting solutions were spread onto the NMP pre–wetted PET substrates by a 50 µm casting knife (Elcometer 3530), followed by immersed them in the IPA coagulation baths for 18 h. The IPA coagulation baths contained the 5 wt% HDA and 4 wt% Hmim. The as–prepared support layers were defined as SIM_{ISG}–X (X = 0.5, 1, 1.5, and 2.5) series, where X corresponds to the loading of $Zn(NO_3)_2•6H_2O$ in wt.%. The prepared solvent–resistant PI support layer without ZIF–8 nanocrystals was defined as SIM for blank sample.

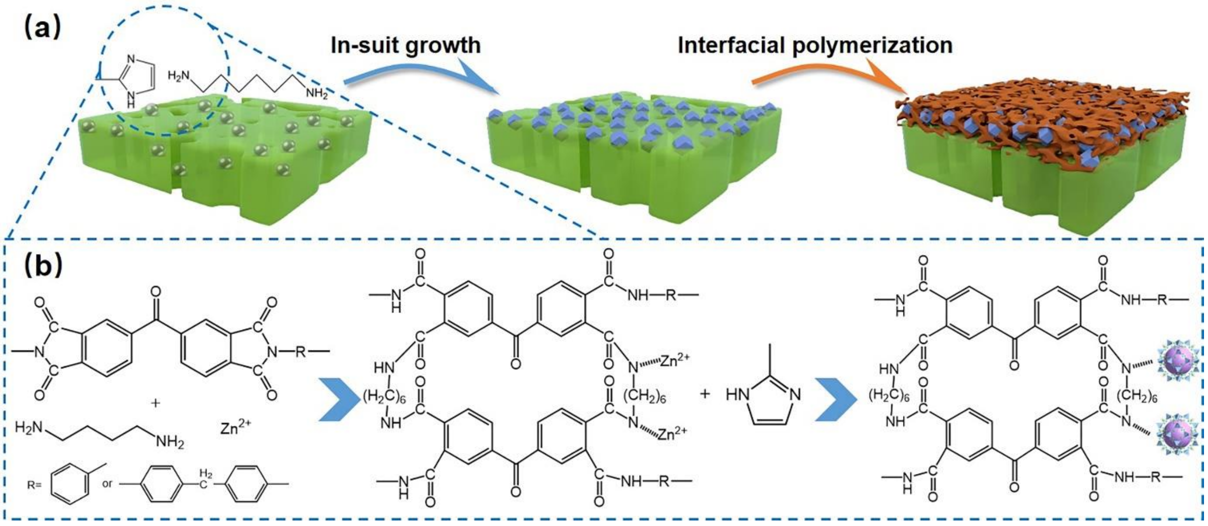

Fig. 1 (a) Schematic illustration of the fabrication of TFNi membranes featuring an interlayer of ZIF–8 nanocrystals, (b) Potential mechanism including the crosslinking reaction and the nucleation of ZIF–8 nanocrystals.

Table 1 The key parameters of casting solutions and coagulation baths.

Support layers	**Casting solutions (wt%)**				**Coagulation baths (wt%)**		**Zn^{2+}: Hmim**
	PI	PEG400	NMP	$Zn(NO_3)_2•6H_2O$	HDA	Hmim	
SIM	12	0.5	87.5	0	5	0	–
SIM_{ISG}–0.5	12	0.5	87.0	0.5	5	4	1:333
SIM_{ISG}–1.0	12	0.5	86.5	1.0	5	4	1:165
SIM_{ISG}–1.5	12	0.5	86.0	1.5	5	4	1:109

SIM_{ISG}–2.5	12	0.5	85.0	2.5	5	4	1:65

2.2.2 Preparation of PA rejection layer

The PA rejection layer was fabricated by the interfacial polymerization reaction of MPD (3.4 wt% in DI water solution) and TMC (0.3 wt% in Isopar–G solution). First, the prepared support layers were immersed in the MPD solution for 120 s, and then the MPD–wetted support layers were immersed in the TMC Isopar–G solution for 60 s to initiate the interfacial polymerization reaction. In order to improve the interfacial polymerization [49], the obtained PA rejection layers were heated at 100 °C for 300 s and the prepared TFNi membranes stored in EtOH at 4 °C. These TFNi membranes on the SIM and SIM_{ISG}–X support layers were defined as OSFO and $OSFO_{ISG}$–X, respectively.

2.3 Characterization of membranes

X–ray diffraction (XRD, D8 ADVANCE, Bruker) was used to discriminate ZIF–8 nanocrystals in the support layers. Attenuated total reflection infrared spectroscopy (ATR–FTIR, VERTEX 70, Bruker) was employed to evaluate the functional group of support layers. The morphologies of ZIF–8 nanocrystals, support layers, and TFNi membranes were proposed by scanning electron microscopy (SEM, Nova NanoSEM 450). Prior to test, membrane coupons were freeze–dried by a vacuum freezing and drying technology (FreeZone6.0, LABCONCO) and coated with gold using a sputtering coater (MCIOOO ION SPUTTER). A transmission electron microscope (TEM, FEI Technai G2) was used to evaluate the cross–sectional morphologies of TFNi membranes. The preparation protocols are briefly presented as follows: membranes were embedded in a resin (Poly/Bed® 812, Warrington, PA) and were further sectioned by approximately 100 nm in thickness onto a copper grid by an Ultracut E ultramicrotome (Reichert, Inc. Depew, NY). Surface composition and crosslinking degree of PA rejection layers were evaluated by X–ray photoelectron spectroscopy (XPS, Thermo ESCALAB 250XI). Hydrophilicity of the support layers was evaluated at room temperature by a contact angle meter (DSA100, Krüss). A capillary flow porometry (CFP, Beishide 3H–2000PB) was proposed to measure the pore sizes distribution of support layers via the gas–liquid displacement. The surface roughness of support layers and TFNi membranes were characterized using atomic force microscope (AFM, NanoScope V MultiMode8, Bruker) with the tapping mode. The thermal stability of support layers was demonstrated using a thermogravimetric analyzer (TGA, NETZSCH–STA 2500 Regulus) with a heating rate of 10 °C min^{-1} from 50 to 800 °C under an air flow of 50 mL min^{-1}. The overall porosity (ε) of support layers was calculated with the following equation (1):

$$\varepsilon = \frac{\left(m_{wet} - m_{dry}\right)/\rho_w}{\left(m_{wet} - m_{dry}\right)/\rho_w + \left(m_{dry}/\rho_p\right)} \times 100\% \qquad (1)$$

where m_{wet} indicates wet mass, m_{dry} indicates dry mass, ρ_w indicates water density, and ρ_p indicates polymer density.

2.4 Solvent permeance performance of TFNi membranes with ZIF–8 interlayer

2.4.1 Intrinsic properties

Water and solvents permeance of support layers and TFNi membranes were measured by a dead–end RO filtration system (HP4750, Sterlitech) under room temperature using the following equation (2). The solvents permeance (A, L m^{-2} h^{-1} bar^{-1}) of TFNi membranes was calculated under a constant applied pressure (ΔP) of 8 bar as follows equation (3):

$$J_e = \frac{\Delta V}{A_m \Delta t} \tag{2}$$

$$A = \frac{J_e}{\Delta P} \tag{3}$$

where J_e represents permeation flux, ΔV represents the permeate volume change through the effective membrane area (A_m) of 14.6 cm^2, Δt represents the time interval.

The various ethanol solutions containing 100 mg L^{-1} PS with different molecular weight were used as the feed solutions. The molecular weight cut–off (MWCO) of TFNi membranes was calculated as follows equation (4):

$$R = \left(1 - \frac{C_p}{C_f}\right) \times 100\% \tag{4}$$

where C_f and C_p are the concentration of PS in the feed and permeation, respectively. An ultraviolet and visible spectrophotometer (UV–Vis, TU–1810, PERSEE) was used to measure the concentrations of PS in ethanol with an absorption wavelength of 203 nm.

2.4.2 OSFO performance

The OSFO performance of TFNi membranes were evaluated by a lab–scale cross–flow OSFO filtration system (Fig. 2), and the pure ethanol as feed solution (FS) and 1 M LiCl–ethanol solution as draw solution (DS). The flow rate of membrane surfaces was controlled at 2.2 cm s^{-1} under room temperature and the effective membrane area (A_m) was 9 cm^2. The prepared TFNi membranes were operated under FO mode (PA rejection layer facing FS) and PRO mode (PA rejection layer facing DS), respectively. The ethanol (J_e, L m^{-2} h^{-1}) and reverse LiCl (J_s, g m^{-2} h^{-1}) fluxes were used to evaluate the OSFO performance of TFNi membranes, as follows equations (5) and (6):

$$J_e = \frac{\Delta M}{\rho A_m \Delta t} \tag{5}$$

$$J_s = \frac{\Delta C_t V_t}{A_m \Delta t} \tag{6}$$

where ΔM is the mass change of DS over a time interval Δt. ρ represents the ethanol density. ΔC_t is the change of LiCl concentration and V_t is the volume of FS measured at the end of tests.

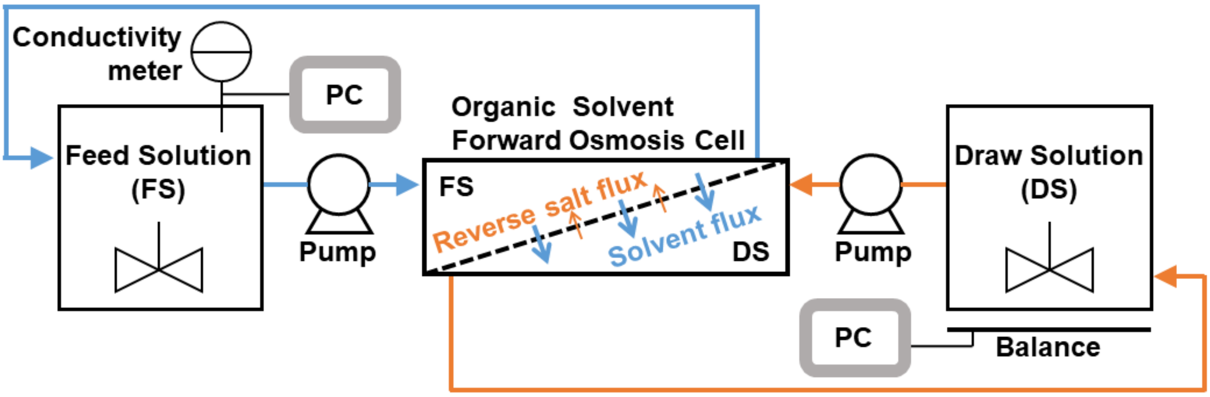

Fig. 2 The flow diagram of the lab–scale cross–flow OSFO filtration system.

The influence of internal concentration polarization (ICP) of TFNi membranes during the OSFO process was indicated by the structural parameter (*S*) [4, 43], which can be calculated by equation (7) under FO mode. The LiCl permeance (*B*) was calculated by equation (8) according to the solution–diffusion model [4, 50].

$$S = \frac{D}{J_e}\left[\ln \frac{A\pi_{draw} + B}{A\pi_{feed} + B + J_e}\right] \tag{7}$$

$$B = \frac{J_s}{J_e} A \bullet iRT \tag{8}$$

where π_{draw} and π_{feed} are the osmotic pressure of DS and FS, respectively. J_e and A are the ethanol flux and permeance of TFNi membranes, respectively. D is the diffusion coefficient of LiCl in ethanol, i represents the van't Hoff factor, which is assumed to be 1 in this study. R is the gas constant, and T represents the absolute temperature.

The diffusion coefficient (D value) was calculated by equation (9) according to the verified Stokes−Einstein relationship [51].

$$D = \frac{kT}{4\pi\eta r_i} \tag{9}$$

where k represents Boltzmann's constant. π represents the ratio of circumference to diameter. η represents the solution viscosity, and r_i represents the radius of the solute. The legend explanations of equations were shown in Table S1.

3 Results and discussion

3.1 Characterization of solvent–resistant PI support layers with ZIF–8 nanocrystals.

When adding Zn^{2+} and Hmim into the casting solutions and coagulation bath respectively, the phase–inversion of PI support layer, the crosslinking of PI polymer, and the nucleation of ZIF–8 nanocrystals simultaneously occurred by the novel ISG strategy. The XRD patterns (Fig. 3(a)) demonstrated the successful preparation of ZIF–8 nanocrystals in the novel ISG process. Compared with the SIM support layer, the XRD characteristic peaks of ZIF–8 nanocrystals for the SIM_{ISG}–X series gradually appeared with increasing the Zn^{2+} concentration. The characteristic peaks at 7.4, 10.3, and 12.7 (2 theta degrees) of SIM_{ISG}–2.5 support layer could be indexed to the ZIF–8 phase (CCDC 864309) [52], confirming the well–developed structure of ZIF–8 with high crystallinity [53]. To further confirm the functional groups of support layers, the ATR–FTIR spectra were conducted as shown in Fig. 3(b). The characteristic peaks of prepared support layers at 1647 cm^{-1} (C=O stretching) and 1540 cm^{-1} (C–N stretching), correspond to the typical amide group of PI polymer after the

HDA crosslinking [54, 55]. Also, the characteristic peaks of SIM_{ISG}–X series at 421 cm^{-1} (Zn–N), 687 and 761 cm^{-1} (ring out–of–plane bending), and 995, 1145 and 1179 cm^{-1} (ring in–plane bending) gradually appeared with increasing the Zn^{2+} concentration, consistent with the characteristic peaks of ZIF–8 nanocrystals [56, 57].

In addition, the thermogravimetry (TG) curves and its first derivative (DTG) curves of synthesized ZIF–8 nanocrystals and prepared support layers were shown in Fig. 3(c) and (d). A weak weight loss of synthesized ZIF–8 nanocrystals before 400 °C was attributed to the elimination of water molecules. Another apparent weight loss of synthesized ZIF–8 nanocrystals between 400 and 600 °C was obtained, which was ascribed to the decomposition of ZIF–8 into ZnO [58]. Both the SIM and SIM_{ISG}–X series support layers have three stages of weight loss, which were attributed to the loss of adsorbed water, the decomposition of amide groups, and the decomposition of PI polymer chains, respectively [43, 59]. The degradation temperature of pure ZIF-8 nanocrystals was ~425 °C, and the degradation temperature of SIM support layer was ~540 °C. With increasing the Zn^{2+} loadings, the additional ZIF–8 nanocrystals were generated in the SIM_{ISG}-X series support layers, thus resulting in the decrease of degradation temperature. [60]. In addition, the amount of ZIF–8 in the SIM_{ISG}–X series support layers were estimated by the TGA analyses. The mass ratios of ZIF–8 nanocrystals in the prepared SIM_{ISG}–0.5, SIM_{ISG}–1.0, SIM_{ISG}–1.5 and SIM_{ISG}–2.5 support layers were about 0.11, 3.21, 3.33 and 6.90 %, respectively.

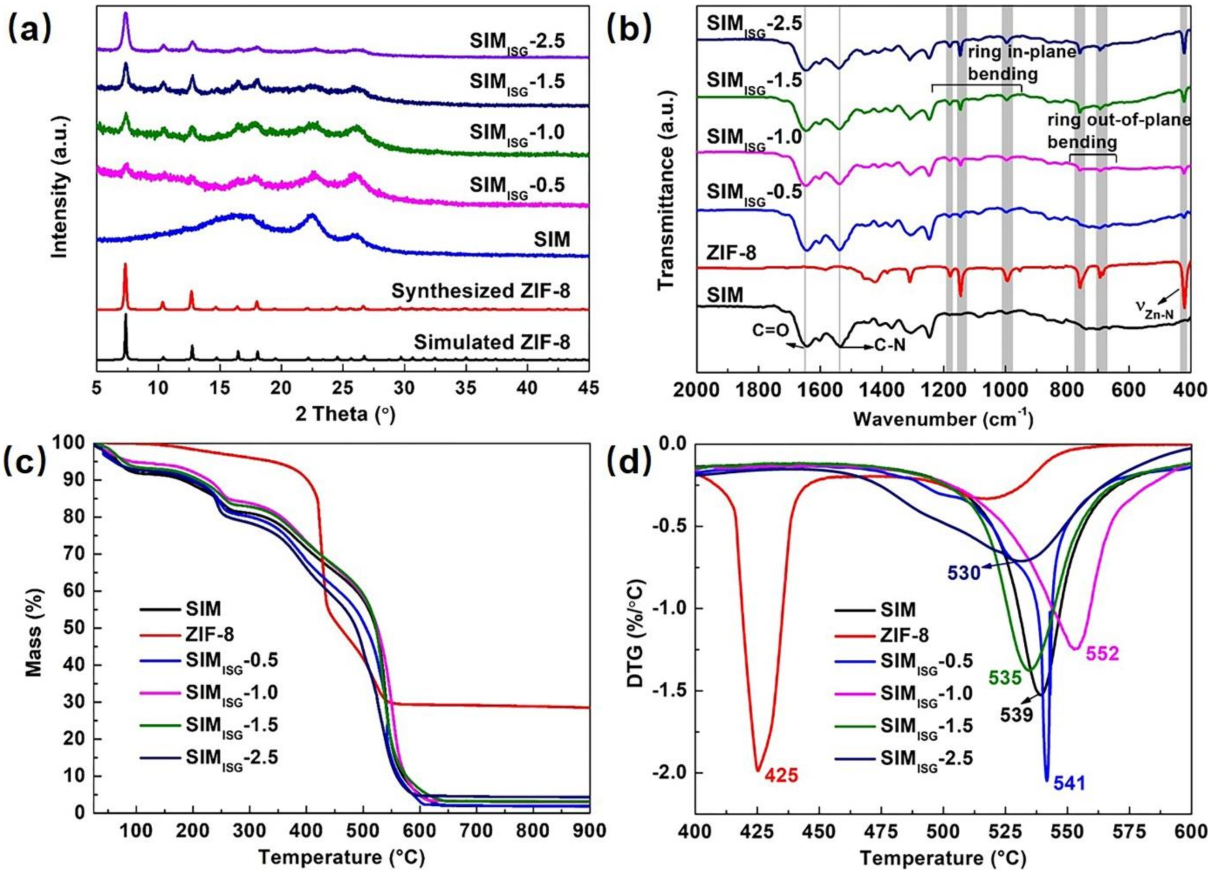

Fig. 3 (a) XRD patterns, (b) ATR–FTIR spectra, (c) TG and (d) DTG curves of the ZIF–8 nanocrystals, SIM and SIM_{ISG}–X series support layers.

The novel ISG strategy of ZIF–8 nanocrystals played an important role in the support layers formation process by the modified SIM method. The HDA not only is a crosslinking agent for crosslinked PI support layer, but also immobilizes Zn^{2+} to promote the nucleation of ZIF–8 in the modified SIM method [61]. When the coagulation bath contains both the HDA and Hmim, the clarified coagulation bath was obtained (see Fig. S1) compared with the coagulation bath only has Hmim. Fig. 4(a) showed the overall porosity and contact angle of the resultant support layers. The introduction of ZIF–8 nanocrystals slightly reduced the overall porosity of support layers. For example, the porosity of SIM_{ISG}–0.5 support layer was 71 %, which was lower than that of SIM support layer (76%). However, increasing the concentration of Zn^{2+}, the additional ZIF–8 nanocrystals were generated thus resulting in the increase of overall porosity of SIM_{ISG}–X series. Moreover, the SIM_{ISG}–X series support layers demonstrated the higher water contact angles as compared with the SIM support layer, due to the hydrophobicity property of the distributed ZIF–8 nanocrystals on the surfaces [62, 63]. In addition, compared with the SIM support layer, the surface roughness of SIM_{ISG}–X series were significantly improved (Fig. 4(b)), which is in good agreement with the larger nodular structure of surfaces by nucleation of ZIF–8 nanocrystals.

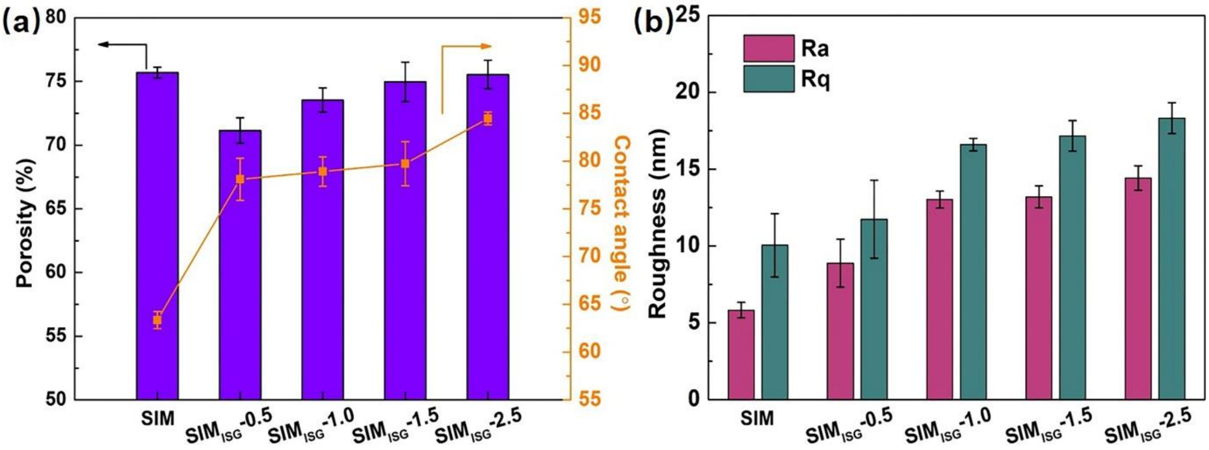

Fig. 4 (a) Contact angle and overall porosity, (b) surface roughness of the SIM and SIM_{ISG}–X series support layers.

3.2 Effects of ZIF–8 nanocrystals on the morphology of the support layers

The morphology of as–prepared support layers was investigated by SEM characterization as shown in Fig. 5 and Fig. 6. Fig. 5(a) shows that the synthesized ZIF–8 nanocrystals had a "cubic" shape with a particle size of ~50 nm, the BET surface area of 1139 m^2 g^{-1}, and the micropore volume of 0.58 cm^3 g^{-1} by N_2 adsorption–desorption isotherms. The pore width distributions of synthesized ZIF–8 nanocrystals were calculated based on the BJH method as shown in Fig. S2, and most of the micropores showed diameter below 1 nm. The effect of

Zn^{2+} concentration on the surface morphology of support layers was shown in Fig. 5(b-f). The SIM support layer (Fig. 5(b)) showed a porous surface and the porosity of surface was ~2.68%. With the introduction of Zn^{2+} and Hmim in the modified SIM process, the surfaces of SIM_{ISG}–X series support layers became more porous (e.g., the surface porosity of SIM_{ISG}–2.5 was ~4.16%) and the obtained ZIF–8 nanocrystals were uniformly distributed on the surfaces (Fig. 5(c–f)). These observations suggest that the migration of Zn^{2+} induced greater porosity and the nucleation of ZIF–8 nanocrystals on the interfaces [37, 64, 65]. As the concentration of Zn^{2+} (enhanced the ZIF–8 nucleation sites) increased, a wider particle distribution of ZIF–8 nanocrystals on the surfaces were obtained, e.g., the average particle sizes of ZIF–8 on the SIM_{ISG}–2.5 surface was 38.20 ± 8.86 nm, which facilitated an enhanced influence of the ZIF–8 interlayer on the permeance as discussed section 3.4.

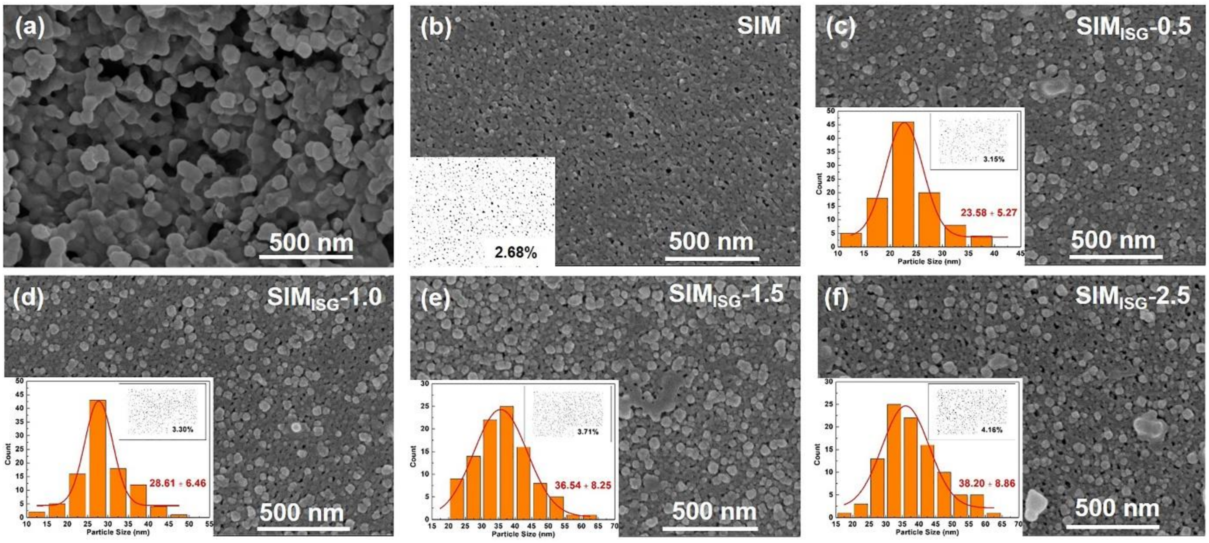

Fig. 5 Surface morphology of the ZIF–8 nanocrystals, SIM and SIM_{ISG}–X series support layers. (a) synthesized ZIF–8 nanocrystals, (b) SIM, (c) SIM_{ISG}–0.5, (d) SIM_{ISG}–1.0, (e) SIM_{ISG}–1.5, and (f) SIM_{ISG}–2.5 support layers. Surface porosity of support layers and the particle size distribution of ZIF–8 nanocrystals on the surfaces were demonstrated by ImageJ analysis.

The effect of Zn^{2+} concentration on the cross–sectional morphology of support layers is shown in Fig. 6. The support layers presented finger–like porous structure underneath a dense skin layer. However, the SIM_{ISG}–0.5 support layer had more prevailing sponge–like skin (Fig. 6(b)). Despite this exception, it can be explained by the interaction between unsaturated Zn^{2+} of ZIF–8 and functional groups of crosslinked PI, which reduced the phase–inversion rate of support layers [66]. In order to understand this exception, we prepared the four solvent–resistant PI support layers with different $Zn(NO_3)_2{\bullet}6H_2O$ concentration (0.5, 1.0, 1.5, and 2.5 wt%) without Hmim in the coagulation baths as shown in Fig. S3(a–d). The sponge–like pores almost covered the cross–sectional of solvent–resistant PI support layer with 0.5 wt% $Zn(NO_3)_2{\bullet}6H_2O$ concentration (Fig. S3(a)). As increasing the concentration of $Zn(NO_3)_2{\bullet}6H_2O$, the sponge–like pores were gradually restricted and the finger–like pores prevailed, e.g., the finger–like pores through the solvent–resistant PI support layer with 2.5 wt% $Zn(NO_3)_2{\bullet}6H_2O$ concentration (Fig. S3(d)) was obtained. This change should be ascribed to the migration of Zn^{2+}, which accelerated the precipitation rate of PI polymers during phase–inversion process.

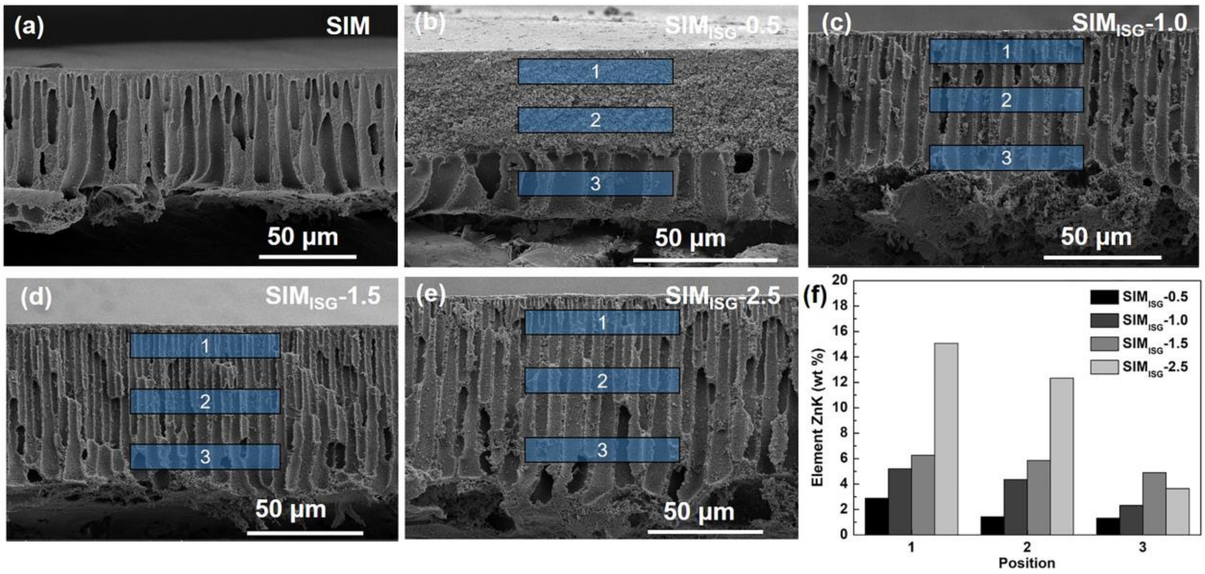

Fig. 6 Cross–sectional morphology of the SIM and SIM_{ISG}–X series support layers. (a) SIM, (b) SIM_{ISG}–0.5, (c) SIM_{ISG}–1.0, (d) SIM_{ISG}–1.5, and (e) SIM_{ISG}–2.5 support layers. (f) The loadings of Zn in the different locations of the above support layers were analyzed by EDX mapping.

In addition, Fig. S4 showed the pore size distributions of support layers. The average pore size of SIM support layer was 116.3 nm. After the introduction of ZIF–8 nanocrystals in the solvent–resistant PI support layers, except the SIM_{ISG}–0.5 support layer, the average pore sizes of SIM_{ISG}–X series were significantly improved, e.g., the average pore size of SIM_{ISG}–2.5 support layer was 173.6 nm. Furthermore, the loadings of Zn in the different locations of support layers were analyzed by EDX mapping as shown in Fig. 6(f). A certain amount of Zn was found at all three tested positions of the SIM_{ISG}–X series support layers. The Zn loading of position 1 was generally higher than that of positions 2 and 3. In particular, the Zn loading of position 1 of the SIM_{ISG}–2.5 support layer was about 15 wt%, which was about five times than that of position 3. This distribution of ZIF–8 nanocrystals was benefited by the higher concentration of $Zn(NO_3)_2$•$6H_2O$ (a higher ratio of Zn^{2+}/Hmim), which improved the Zn^{2+} migration into surfaces and enhanced the nucleation of ZIF–8 in the interfaces [65, 67, 68]. Fig. 7 showed the water and ethanol permeances of prepared support layers. The SIM support layer had higher water and ethanol permeances than that of the SIM_{ISG}–X series, attributed to the improved hydrophilicity of surface and the higher porosity (Fig. 4(a)). With increasing the concentration of Zn^{2+}, the water and ethanol permeances of SIM_{ISG}–X series were improved, consistent with the changing trend of the overall porosity and average pore size.

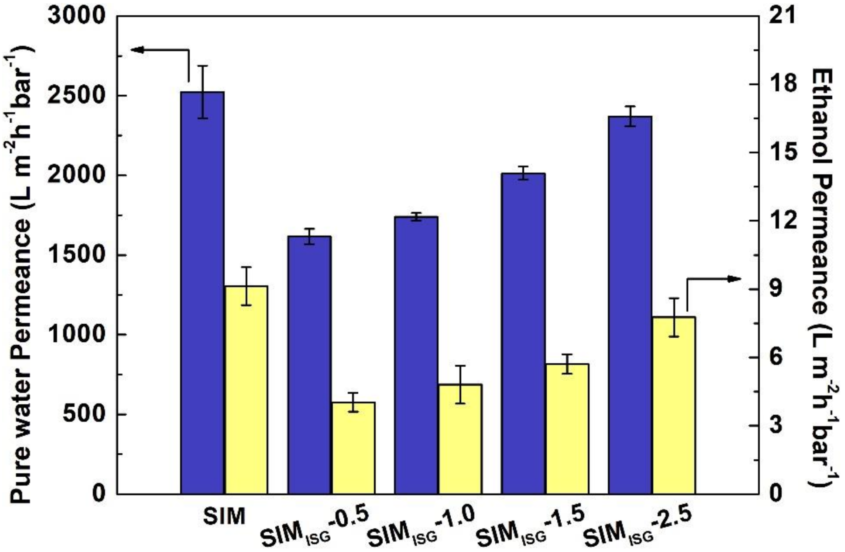

Fig. 7 Water and ethanol permeances of the SIM and SIM_{ISG}–X series support layers under 1 bar applied pressure.

3.3 Characterization of PA layers on the support layers

The ZIF–8 interlayer on the prepared support layers plays an important role to affect the interfacial polymerization reaction [69-71]. The PA layer of OSFO membrane shows the typical “ridge–valley” surface morphology (Fig. 8(a)) with an apparent thickness of ~218 nm

(Fig. 8(d)) and an average roughness of 74.8 nm (Fig. 8(g)). After introduction of ZIF–8 interlayer on the support layers, larger leaf–like PA layers were formed for the $OSFO_{ISG}$–X series membranes as shown in Fig. 8(b, c) and Fig. S5(a, b). This change contributes to enhancing the apparent thickness and roughness of the PA layers [43], e.g., the apparent thickness (Fig. 8(e)) and roughness (Fig. 8(h)) of the PA layer of $OSFO_{ISG}$–0.5 membrane were ~259 nm and ~127.67 nm, respectively. The increased roughness of the $OSFO_{ISG}$–X series membranes can be potentially ascribed to the confinement effect, where the preloaded ZIF–8 interlayer could confine the nanobubbles that are generated during the interfacial polymerization reaction [26, 72, 73]. It is worthwhile to note that the more uniform ZIF–8 nanocrystals as the interlayer of support layers with higher surface porosity (Fig. 5) were obtained, due to the increased concentration of Zn^{2+}. The ZIF–8 nanocrystals interlayer and porous surfaces could facilitate the MPD diffusion into the organic phase for promoting the interfacial polymerization reaction, and thus creating a more rigid PA layer [37, 73, 74], e.g., the apparent thickness (Fig. 8(f)) and roughness (Fig. 8(i)) of the PA layer of $OSFO_{ISG}$–2.5 membrane were ~182 nm and ~76.33 nm, respectively.

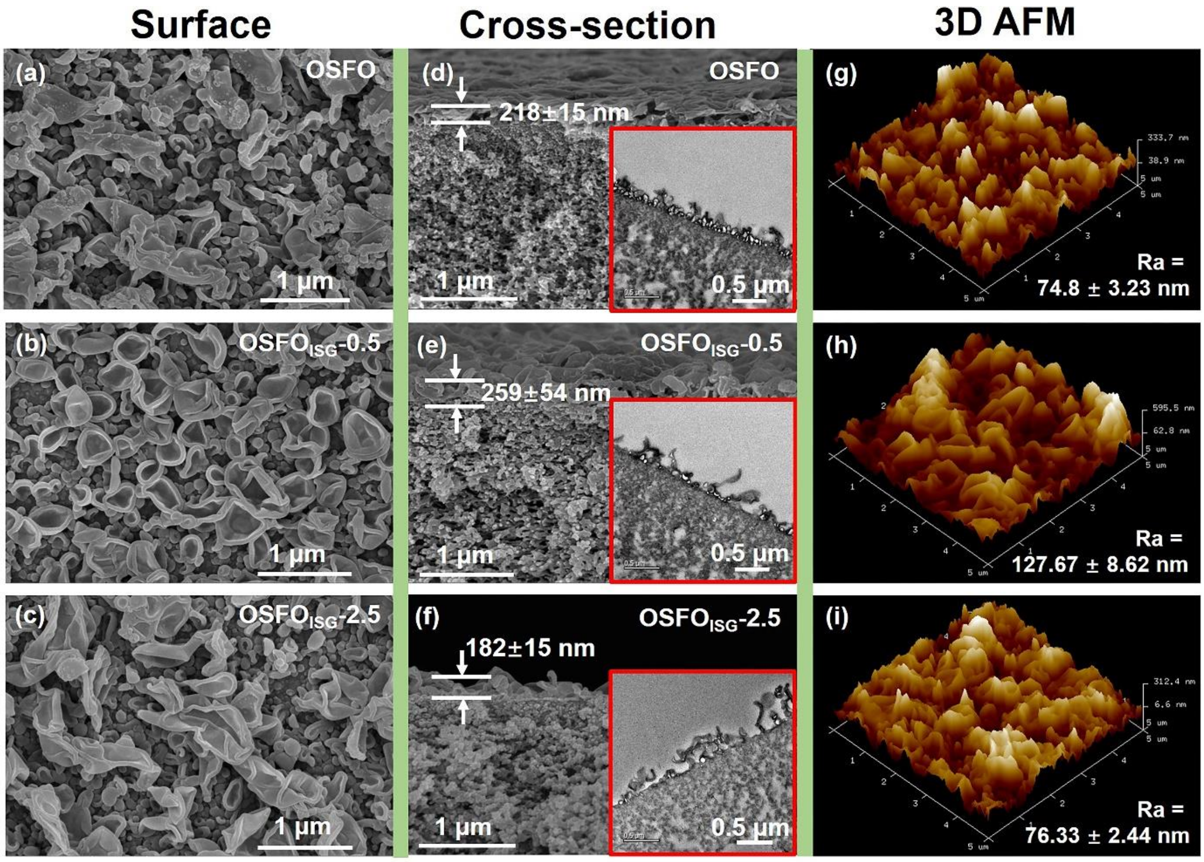

Fig. 8 Surface (a–c) and cross–sectional (d–f) morphologies, and 3D–AFM images (g–i) of the PA layer on the SIM, SIM_{ISG}–0.5, and SIM_{ISG}–2.5 support layers.

XPS spectra were utilized to analyze the element composition of PA layers (Fig. 9(a)). Three deconvolution peaks of C1s, N1s, and O1s for OSFO and $OSFO_{ISG}$–X series membranes were observed through XPS spectra (Fig. 10) and the results were shown in Table S2. From the C1s spectra, four main peaks were observed at 287.9, 286.1, 285.8 and 284.6 eV, which can correspond to C=O, C–O, C–N (C=N) and C–C (C–H) groups from the PA layer, respectively [75, 76]. In addition, the ratios of O–C=O ascribed to the hydrolysis of unreacted acyl chloride groups and $–NH_2$ is originating from the unreacted amine groups [77], which could also be estimated from the O1s and N1s high resolution spectra (Fig. 10 and Table S2). Compared with the OSFO membrane, the $OSFO_{ISG}$–X series membranes show the presence of Zn at 1046 ($2p_{1/2}$) and 1022 eV ($2p_{3/2}$). Fig. 9(b) shows the O:N ratio based on the XPS results and the calculated crosslinking degree of PA layers. Only marginal changes could be identified for Zn^{2+} loading up to 1.5 wt.%, with O:N ratio ranging from 1.14–1.17. However, the $OSFO_{ISG}$–2.5 membrane had a much lower O:N ratio of 1.08, corresponding to a higher crosslinking degree [26] of 89% compared to 80.5% for OSFO membrane. With increasing Zn^{2+} loadings, more Zn^{2+} ions would coordinate the Hmim and heterogeneous nucleation of ZIF–8 nanocrystals on support layer surface (Fig. 5). The acquired ZIF–8 nanocrystals can adsorb more MPD monomers, and the porous structures can provide the more reaction spaces between polyamide and ZIF–8 [78], resulting in accelerating diffusion of MPD into the organic phase and improving the crosslinking of PA layer.

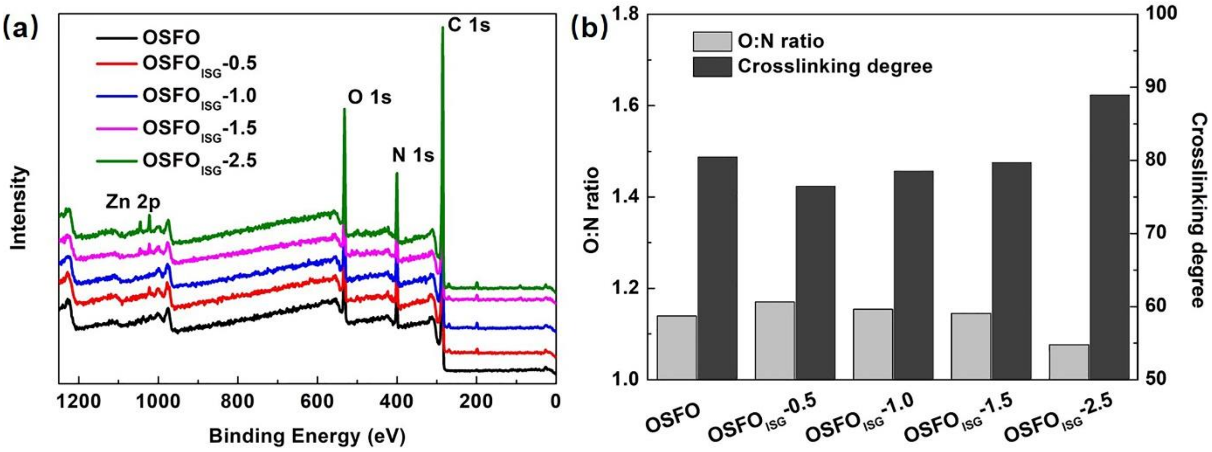

Fig. 9 (a) XPS spectra of the PA layers on the as–prepared support layers, (b) the oxygen/nitrogen ratio ($r_{O/N}$) and crosslinking degree of PA layers from the XPS results analyzed by the equation ($4-2r_{O/N}$)/($1+r_{O/N}$) [26].

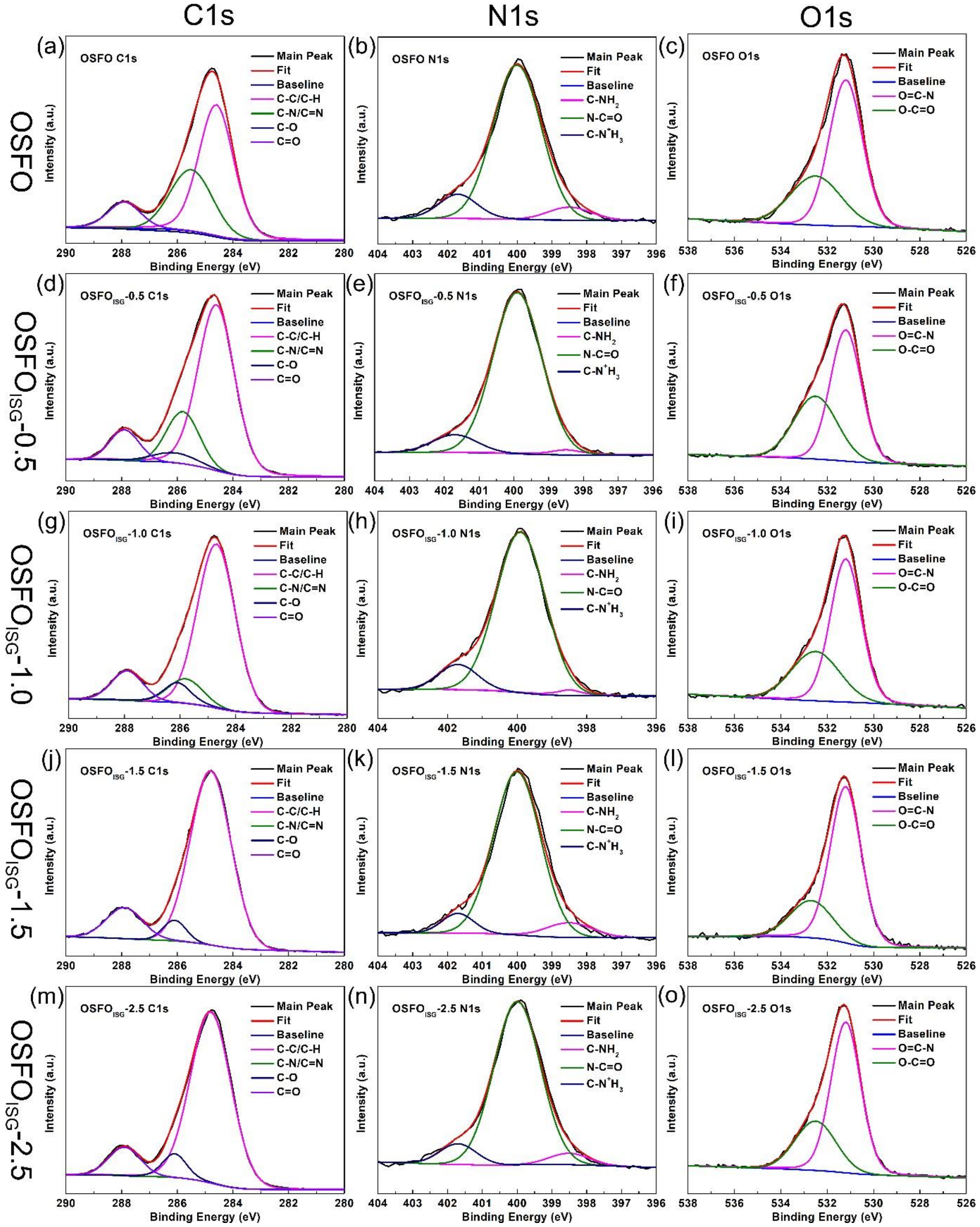

Fig. 10 High–resolution and deconvolution of C1s, N1s and O1s XPS spectra of the OSFO (a–c), OSFO$_{ISG}$–0.5 (d–f), OSFO$_{ISG}$–1.0 (g–i), OSFO$_{ISG}$–1.5 (j–l) and OSFO$_{ISG}$–2.5 (m–o) membranes, respectively.

3.4 The impact of ZIF–8 interlayer on the performance of TFNi membranes

3.4.1 Solvent permeances and MWCO of TFNi membranes

Fig. 11 showed the ethanol permeance performance and PS rejection of obtained TFNi membranes. The ZIF–8 interlayer–incorporated $OSFO_{ISG}$–X series membranes (Fig. 11(a)) showed effective enhancement of ethanol permeance, e.g., 0.47 ± 0.03 L m^{-2} h^{-1} bar^{-1} for the $OSFO_{ISG}$–2.5 membrane compared to 0.34 ± 0.03 L m^{-2} h^{-1} bar^{-1} for the OSFO membrane. With increasing the concentration of Zn^{2+}, the ethanol permeances of $OSFO_{ISG}$–X series were improved, which can be attributed to greater ZIF–8 loading and more nanochannels incorporated in the TFNi membranes. The N,N–dimethylformamide (DMF) activation plays an important impact on the permeance of PA layer [25]. The ethanol permeance of obtained TFNi membranes were significantly improved after 10 h DMF activation, e.g., the ethanol permeance of $OSFO_{ISG}$–2.5 membrane reached 0.74 ± 0.05 L m^{-2} h^{-1} bar^{-1}. In addition, the molecular weight cut–off (MWCO) of OSFO and $OSFO_{ISG}$–2.5 with or without DMF activation was evaluated (Fig. 11(b)). Compared with the MWCO of OSFO membrane, the $OSFO_{ISG}$–2.5 membrane had decreased MWCO and enhanced PS rejection, which is consistent with its formation of a more crosslinked PA layer (see Fig. 9(b)). After the 10 h DMF activation, there was no significant change in the MWCO curves, confirming the stability of obtained TFNi membrane by the novel ISG strategy. Additionally, the novel ISG strategy significantly reduced the agglomeration of ZIF–8 nanocrystals (Fig. 5), thereby avoiding the generation of possible non–selective defects in the resulting TFNi membranes.

Various solvents were used to investigate the permeance of OSFO and $OSFO_{ISG}$–2.5 membranes (Fig. 11(c)), and the properties of various solvents were summarized as shown in

Table S3. For the DI–water, all of the prepared membranes showed the highest permeances, which due to the maximum solubility parameter and minimum kinetic diameter, e.g., the DI–water permeance of $OSFO_{ISG}$–2.5 membrane reached 9.73 L m^{-2} h^{-1} bar^{-1}. For the alcohols, the permeance order follows the sequence of MeOH > EtOH > IPA, which obeys the exact order of their MWs, viscosity and kinetic diameter [79] (Table S3). For the n–Hexane, hardly any permeance is observed due to high hydrophilicity of the membrane surface, e.g., δ_p is 0 $MPa^{1/2}$ [80]. All of the above solvent's permeances were proportional to the solvent properties, however the special one is THF, the solvent activation and the interactions between THF and membrane materials primarily affect the permeation behavior of THF, then the prepared membranes showed the higher permeance [81]. Similarly, the various solvent permeances of TFNi membranes were significantly improved after 10 h DMF activation, e.g., the DI–water and THF permeances of $OSFO_{ISG}$–2.5 membrane reached 16.94 and 6.62 L m^{-2} h^{-1} bar^{-1}, respectively. Based on the "gutter effect" [22, 26], the ZIF–8 interlayer could act as a high–permeability gutter layer, which could greatly reduce the effective transport distance through the low–permeability PA rejection layer (Fig. 12), therefore enhancing the overall transport efficiency of TFNi membranes.

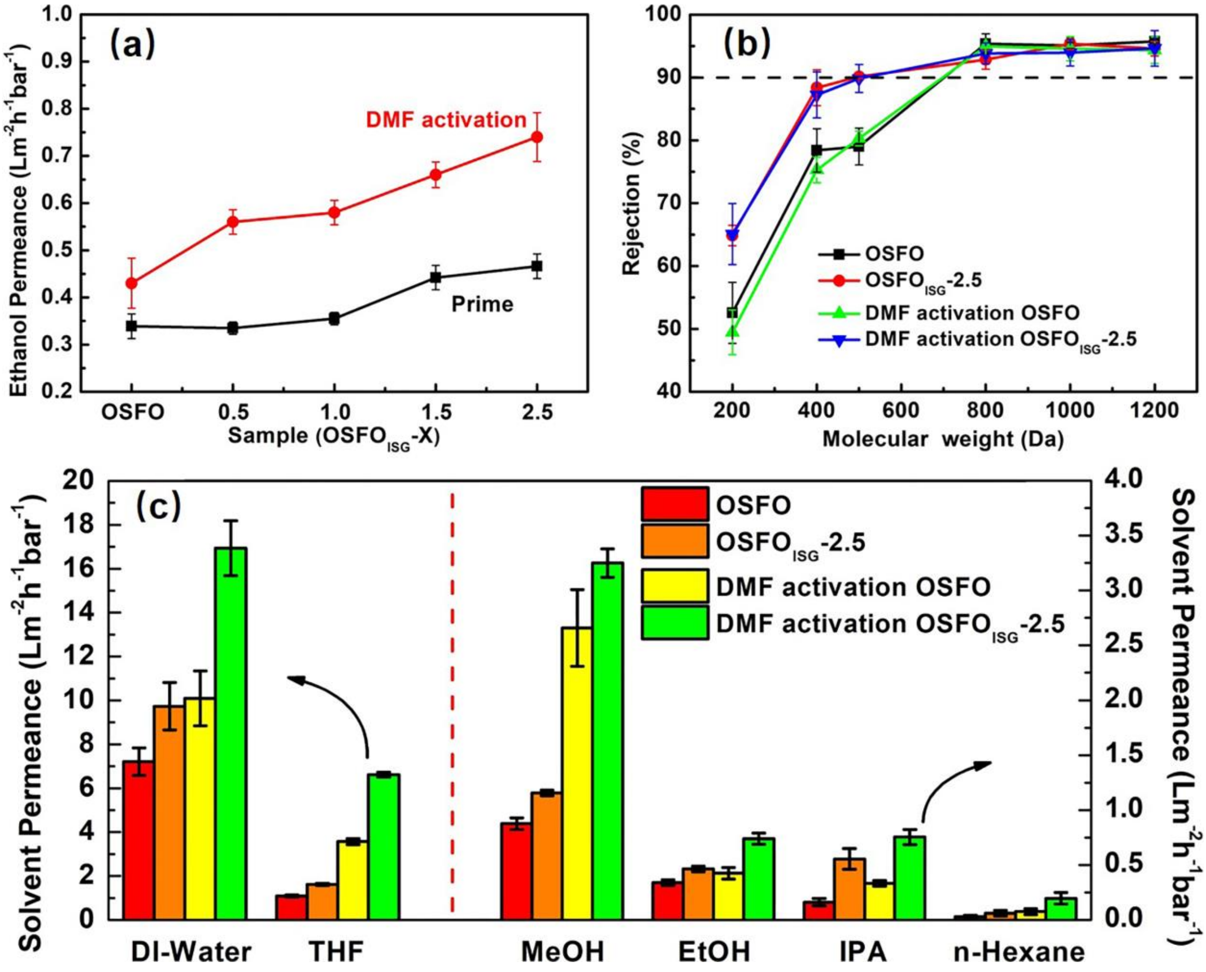

Fig. 11 (a) Ethanol permeance of TFNi membranes with different Zn^{2+} loadings and before and after the 10 h DMF activation, (b) the molecular weight cut–off of typical TFNi membranes before and after the 10 h DMF activation, and (c) the different types of solvents were used to estimate the permeance of typical TFNi membranes before and after the 10 h DMF activation.

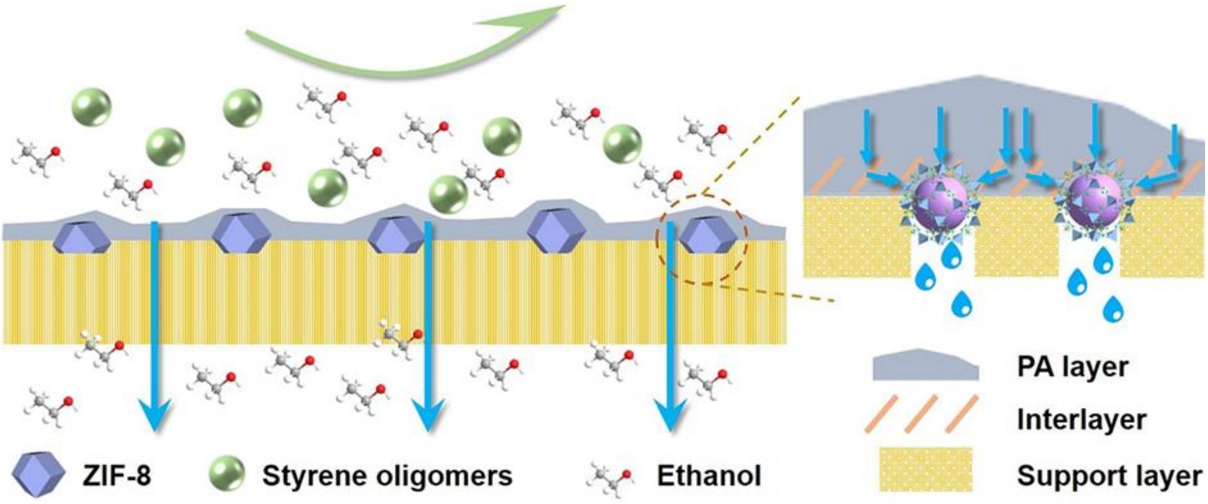

Fig. 12 Schematic illustration of the transport paths in the TFNi membranes.

3.4.2 OSFO performance of TFNi membranes

The OSFO performance of obtained TFNi membranes were also performed using a 1 M LiCl–ethanol draw solution under the FO and PRO modes (Fig. 13). Compared with the OSFO membrane (1.05 ± 0.21 LMH in FO mode and 1.49 ± 0.09 LMH in PRO mode), the ZIF–8 interlayer effectively improved the ethanol fluxes, e.g., the ethanol fluxes of $OSFO_{ISG}$–2.5 membrane were 2.10 ± 0.11 LMH in FO and 2.97 ± 0.31 LMH in PRO modes. The combined effect of a more porous support layer and the high–permeability gutter layer, resulting in a noteworthy reduction in the structural parameter (*S* value, see Table 2) and relieved the severe ICP. The OSFO performance of TFNi membranes has been significantly improved after the 10 h DMF activation, e.g., the ethanol fluxes of $OSFO_{ISG}$–2.5 achieved 3.29 LMH in FO and 4.34 LMH in PRO modes. This improvement was attributed to the dissolution of the small fragments of PA layer and the reduced groups energy by DMF activation [82]. In addition, the DMF activation showed the quite limited effect on the specific selectivity (*Js/Je*) of TFNi membranes, and excellent specific selectivity of

OSFO$_{ISG}$–2.5 membranes was achieved. For further to evaluate the selectivity of obtained TFNi membranes, the LiCl rejections were estimated under FO mode as shown in Fig. S6. The prepared OSFO membrane exhibited the high rejection of LiCl ~98.6% in the OSFO process. With the increasing of Zn^{2+} loading, the enhanced LiCl rejection of OSFO$_{ISG}$–2.5 membrane was obtained, which was attributed to the increase in crosslinking degree of PA layer. After 10 h DMF activation, the slightly lower LiCl rejections (>95%) were observed for the prepared OSFO and OSFO$_{ISG}$–X series membranes. Hence, the prepared ZIF–8 interlayer–incorporated TFNi membranes exhibited the promising OSFO performance compared to the OSFO performance reported in the literature (Table 2).

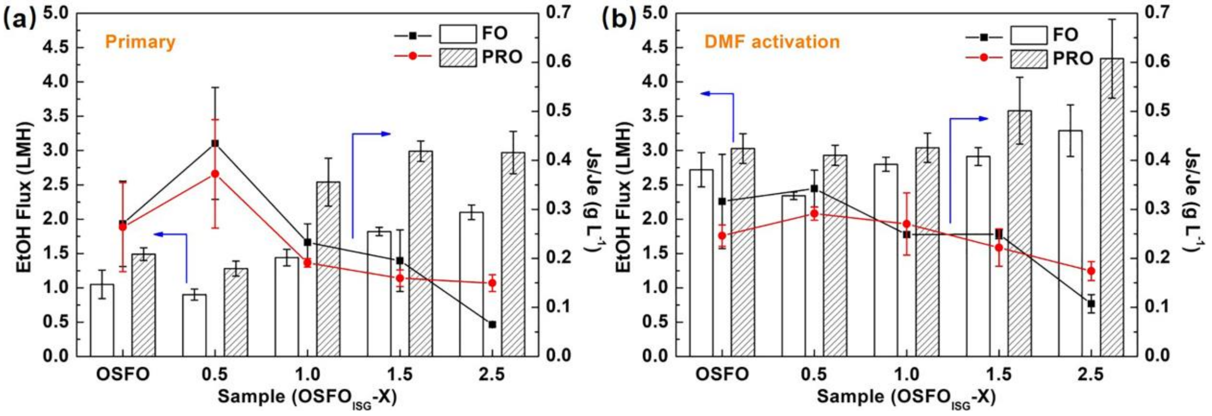

Fig. 13 (a) Ethanol fluxes and specific selectivity (*Js/Je*) of TFNi membranes under FO and PRO modes before and (b) after the 10 h DMF activation.

We compared the relevant literatures on the OSFO and OSN membranes as shown in Table 2. Although the prepared OSFO$_{ISG}$–2.5 membrane exhibited a mediocre ethanol permeance (0.74 ± 0.05 L m^{-2} h^{-1} bar^{-1}) and PS rejection compared with the reported OSN membranes, a more reasonable methanol (3.25 ± 0.13 L m^{-2} h^{-1} bar^{-1}) and THF (6.62 ± 0.12 L m^{-2} h^{-1} bar^{-1}) permeances were obtained. In addition, this is the limitation of SIM method. Although the preparation time and process can be significantly reduced, the loss of ethanol permeance. The initially reported ethanol permeance of the OSN membrane prepared by the SIM method was only 0.2 L m^{-2} h^{-1} bar^{-1} [83]. But the prepared $OSFO_{ISG}$–2.5 membrane showed the higher OSFO performance compared with the reported literatures. This is caused by the effect of different nanoparticles on the transmission process [84] and higher crosslinked support layers by modified SIM method [55].

Table 2 Comparison of the OSFO and OSN performance on the reported and prepared membranes.

Membranes	**Draw solution**	**Feed solution**	***Je* (LMH)**	***Js* (gMH)**	**B/A (KPa)**	**S (μm)**	**Ref.**
TFC	2 M LiCl	Ethanol	2.52 ± 0.14	0.34 ± 0.09	28.70	3196.96	[4]
TFN–STCAss–1.5	2 M LiCl	Ethanol	3.38	0.23	5.85	2338.32	[2]
OSFO	1 M LiCl	Ethanol	1.05 ± 0.21	0.27 ± 0.05	13.48 ± 4.35	4830.09 ±631.86	This work
OSFO$_{ISG}$–0.5	1 M LiCl	Ethanol	0.90 ± 0.08	0.39 ± 0.12	25.39 ± 6.68	5928.63 ± 657.21	This work
OSFO$_{ISG}$–2.5	1 M LiCl	Ethanol	2.10 ± 0.11	0.14 ± 0.02	3.80 ± 0.24	3346.64 ± 251.03	This work
OSFO$_{ISG}$–2.5 with 10 h DMF activation	1 M LiCl	Ethanol	3.29 ± 0.25	0.35 ± 0.06	6.28 ± 1.09	1852.59 ± 631.86	This work

Membranes	**Solvent permeances (L m^{-2} h^{-1} bar^{-1})**		**Solute**	**MW of solute (g mol^{-1})**	**Rejection (%)**	**Ref.**
PI/mZIF-8/PA (mZIF-8)	Ethanol	2.76	Rhodamine B	479	99.1	[45]
UiO-66−NH$_2$/cross-linked Matrimid (UiO-66−NH$_2$)	Ethanol	0.88	Rhodamine B	479	92.8	[85]

PSf/PA-SiO_2 (SiO_2)	Ethanol	0.42	Crystal violet	408	92	[86]
TPP/GO/HPEI/PSS (GO)	Ethanol	3.1	Rose Bengal	1017	97	[87]
TFN (rGO-ODA)	Ethanol	4.6	Sunset yellow	452	98.6	[88]
$(PA-COFs/PI)_{XA}$ (SNW-1)	Ethanol	7.98	Rhodamine B	479	99.4	[89]
PDA/PI (PDA)	Ethanol	0.91	Methyl Blue	800	99	[90]
$(PI-GQDs-50/PI)_{XA}$ (GQDs)	Ethanol	2.3	Rhodamine B	479	98.6	[91]
ZIF-8@RMs/PPSU (ZIF-8)	Methanol	3.66	Rose Bengal	1017	96.1	[92]
TFN−ZIF-8 (ZIF-8)	Methanol	2.5 ± 0.6	Polystyrene	500	>95 %	[84]
$OSFO_{ISG}$-2.5	Ethanol	0.47 ± 0.03	Polystyrene	500	80.3 ± 1.2	This work
	Methanol	2.66 ± 0.35				
$OSFO_{ISG}$-2.5 with 10 h DMF activation	Ethanol	0.74 ± 0.05	Polystyrene	500	89.8 ± 2.2	This work
	Methanol	3.25 ± 0.13				

4 Conclusions

In summary, this work highlights the *in–situ* growth (ISG) of ZIF–8 nanocrystals in the simultaneous phase–inversion and crosslinking process. This process integrated the precipitation of polyimide (PI) substrates, crosslinking between the PI and HDA, and generated ZIF–8 nanocrystals through the interfacial diffusion. The results confirmed that controlling the concentration of Zn^{2+} in the casting solutions was critical for the nucleation of ZIF–8 nanocrystals, and the series of ZIF–8 interlayer–incorporated solvent–resistant PI support layers with three ladder–like distribution were obtained. After interfacial polymerization, the higher crosslinking degree and thinner PA layers were obtained on the PI support layers with ZIF–8 nanocrystals. The prepared TFNi membranes exhibited the improved solvents permeance and enhanced PS rejection under RO mode, outstanding ethanol fluxes and excellent specific selectivity under FO and PRO modes. Furthermore, the significant enhancement of solvents permeance was achieved through 10 h DMF activation, e.g., the THF permeance of $OSFO_{ISG}$–2.5 membrane reached 6.62 L m^{-2} h^{-1} bar^{-1} under RO mode, and the ethanol flux of $OSFO_{ISG}$–2.5 membrane was 4.34 ± 0.57 LMH under PRO mode. This study demonstrates concurrently enhanced the solvents permeance and rejection of the solvent resistance TFNi membranes with ZIF–8 interlayer. The *in–situ* growth (ISG) strategy of ZIF–8 interlayer in the SIM process not only effectively avoided the agglomeration of ZIF–8 nanocrystals, but also effectively promoted the transmission of solvent molecules, and provided insight for the synthesis of MOF on the polymer’s matrix for large–scale production.

Acknowledgments

This study is supported by the National Natural Science Foundation of China (21761132009, 21808113), the Zhejiang Provincial Natural Science Foundation (LR18B060002), the State Key Laboratory of Fine Chemicals, Dalian University of Technology (KF 2010), the General Research Project of Zhejiang Provincial Department of Education (Graduate Project) Foundation (Y202045553), and the S&T Innovation 2025 Major Special Programme (No: 2018B10018, 2020Z036) and sponsored by K.C. Wong Magna Fund in Ningbo University.

References

[1] P. Marchetti, M.F.J. Solomon, G. Szekely, A.G. Livingston, Molecular separation with organic solvent nanofiltration: A critical review, Chem. Rev., 114 (2014) 10735-10806.

[2] B. Li, S. Japip, T.S. Chung, Molecularly tunable thin-film nanocomposite membranes with enhanced molecular sieving for organic solvent forward osmosis, Nat. Commun., 11 (2020) 1198.

[3] R.P. Lively, D.S. Sholl, From water to organics in membrane separations, Nat. Mater., 16 (2017) 276-279.

[4] Y. Cui, T.S. Chung, Pharmaceutical concentration using organic solvent forward osmosis for solvent recovery, Nat. Commun., 9 (2018) 1426.

[5] P. Lu, S. Liang, T. Zhou, X. Mei, Y. Zhang, C. Zhang, A. Umar, H. Wang, Q. Wang, Typical thin-film composite (TFC) membranes modified with inorganic nanomaterials for forward osmosis: A review, Nanosci. Nanotechnol. Lett., 8 (2016) 906-916.

[6] X. Wu, M. Ding, H. Xu, W. Yang, K. Zhang, H. Tian, H. Wang, Z. Xie, Scalable $Ti_3C_2T_x$ Mxene interlayered forward osmosis membranes for enhanced water purification and organic solvent recovery, ACS Nano, 14 (2020) 9125-9135.

[7] B.-H. Jeong, E.M.V. Hoek, Y. Yan, A. Subramani, X. Huang, G. Hurwitz, A.K. Ghosh, A. Jawor, Interfacial polymerization of thin film nanocomposites: A new concept for reverse osmosis membranes, J. Membr. Sci., 294 (2007) 1-7.

[8] V. Vatanpour, M. Safarpour, A. Khataee, H. Zarrabi, M.E. Yekavalangi, M. Kavian, A thin film nanocomposite reverse osmosis membrane containing amine-functionalized carbon nanotubes, Sep. Purif. Technol., 184 (2017) 135-143.

[9] M. Amini, M. Jahanshahi, A. Rahimpour, Synthesis of novel thin film nanocomposite (TFN) forward osmosis membranes using functionalized multi-walled carbon nanotubes, J. Membr. Sci., 435 (2013) 233-241.

[10] O. Choi, S. Karki, R.R. Pawar, S. Hazarika, P.G. Ingole, A new perspective of functionalized mwcnt incorporated thin film nanocomposite hollow fiber membranes for the separation of various gases, J. Environ. Chem. Eng, 9 (2021) 104774.

[11] H. Yang, N. Wang, L. Wang, H.-X. Liu, Q.-F. An, S. Ji, Vacuum-assisted assembly of ZIF-8@GO composite membranes on ceramic tube with enhanced organic solvent nanofiltration performance, J. Membr. Sci., 545 (2018) 158-166.

[12] J. Guo, H. Bao, Y. Zhang, X. Shen, J.K. Kim, J. Ma, L. Shao, Unravelling intercalation-regulated nanoconfinement for durably ultrafast sieving graphene oxide membranes, J. Membr. Sci., 619 (2021) 118791.

[13] M.I. Baig, P.G. Ingole, J.-d. Jeon, S.U. Hong, W.K. Choi, H.K. Lee, Water vapor transport properties of interfacially polymerized thin film nanocomposite membranes modified with graphene oxide and GO-TiO_2 nanofillers, Chem. Eng. J., 373 (2019) 1190-1202.

[14] T.V. Plisko, A.S. Liubimova, A.V. Bildyukevich, A.V. Penkova, M.E. Dmitrenko, V.Y. Mikhailovskii, G.B. Melnikova, K.N. Semenov, N.V. Doroshkevich, A.I. Kuzminova, Fabrication and characterization of polyamide-fullerenol thin film nanocomposite hollow fiber membranes with enhanced antifouling performance, J. Membr. Sci., 551 (2018) 20-36.

[15] Y. Xu, G. Peng, J. Liao, J. Shen, C. Gao, Preparation of molecular selective GO/DTiO$_2$-PDA-PEI composite nanofiltration membrane for highly pure dye separation, J. Membr. Sci., 601 (2020) 117727.

[16] M. You, J. Yin, R. Sun, X. Cao, J. Meng, Water/salt transport properties of organic/inorganic hybrid films based on cellulose triacetate, J. Membr. Sci., 563 (2018) 571-583.

[17] H. Dong, L. Wu, L. Zhang, H. Chen, C. Gao, Clay nanosheets as charged filler materials for high-performance and fouling-resistant thin film nanocomposite membranes, J. Membr. Sci., 494 (2015) 92-103.

[18] P. Lu, Y. Wang, L. Wang, Y. Wei, W. Li, Y. Li, C.Y. Tang, Immobilization of sulfonated polysulfone via 2D LDH nanosheets during phase-inversion: A novel strategy towards greener membrane synthesis and enhanced desalination performance, J. Membr. Sci., 614 (2020) 118508.

[19] P. Lu, S. Liang, L. Qiu, Y. Gao, Q. Wang, Thin film nanocomposite forward osmosis membranes based on layered double hydroxide nanoparticles blended substrates, J. Membr. Sci., 504 (2016) 196-205.

[20] P. Lu, W. Li, S. Yang, Y. Liu, Q. Wang, Y. Li, Layered double hydroxide-modified thin–film composite membranes with remarkably enhanced chlorine resistance and anti-fouling capacity, Sep. Purif. Technol., 220 (2019) 231-237.

[21] P. Lu, W. Li, S. Yang, Y. Wei, Z. Zhang, Y. Li, Layered double hydroxides (LDHs) as novel macropore-templates: The importance of porous structures for forward osmosis desalination, J. Membr. Sci., 585 (2019) 175-183.

[22] Z. Yang, P.-F. Sun, X. Li, B. Gan, L. Wang, X. Song, H.-D. Park, C.Y. Tang, A critical review on thin-film nanocomposite membranes with interlayered structure: Mechanisms, recent developments, and environmental applications, Environ. Sci. Technol., 54 (2020) 15563-15583.

[23] Z. Yang, H. Guo, C.Y. Tang, The upper bound of thin-film composite (TFC) polyamide membranes for desalination, J. Membr. Sci., 590 (2019) 117297.

[24] J. Yin, G. Zhu, B. Deng, Graphene oxide (GO) enhanced polyamide (PA) thin-film nanocomposite (TFN) membrane for water purification, Desalination., 379 (2016) 93-101.

[25] S. Karan, Z. Jiang, A.G. Livingston, Sub-10 nm polyamide nanofilms with ultrafast solvent transport for molecular separation, Science, 348 (2015) 1347-1351.

[26] Z. Yang, F. Wang, H. Guo, L.E. Peng, X.-h. Ma, X.-x. Song, Z. Wang, C.Y. Tang, Mechanistic insights into the role of polydopamine interlayer toward improved separation performance of polyamide nanofiltration membranes, Environ. Sci. Technol., 54 (2020)

11611-11621.

[27] M. Kattula, K. Ponnuru, L. Zhu, W. Jia, H. Lin, E.P. Furlani, Designing ultrathin film composite membranes: The impact of a gutter layer, Sci. Rep., 5 (2015) 15016.

[28] Z. Yang, H. Guo, Z.-k. Yao, Y. Mei, C.Y. Tang, Hydrophilic silver nanoparticles induce selective nanochannels in thin film nanocomposite polyamide membranes, Environ. Sci. Technol., 53 (2019) 5301-5308.

[29] C. Yin, S. Fang, X. Shi, Z. Zhang, Y. Wang, Pressure-modulated synthesis of self-repairing covalent organic frameworks (COFs) for high-flux nanofiltration, J. Membr. Sci., 618 (2021) 118727.

[30] Y.S. Li, F.Y. Liang, H. Bux, A. Feldhoff, W.S. Yang, J. Caro, Molecular sieve membrane: Supported metal-organic framework with high hydrogen selectivity, Angew Chem Int Ed Engl, 49 (2010) 548-551.

[31] Y.-S. Li, H. Bux, A. Feldhoff, G.-L. Li, W.-S. Yang, J. Caro, Controllable synthesis of metal–organic frameworks: From MOF nanorods to oriented mof membranes, Adv. Mater., 22 (2010) 3322-3326.

[32] M.B. Gohain, R.R. Pawar, S. Karki, A. Hazarika, S. Hazarika, P.G. Ingole, Development of thin film nanocomposite membrane incorporated with mesoporous synthetic hectorite and MSH@UiO-66-NH_2 nanoparticles for efficient targeted feeds separation, and antibacterial performance, J. Membr. Sci., 609 (2020) 118212.

[33] J. Li, M. Zhang, W. Feng, L. Zhu, L. Zhang, PIM-1 pore-filled thin film composite membranes for tunable organic solvent nanofiltration, J. Membr. Sci., 601 (2020) 117951.

[34] Y. Lu, Z. Qin, N. Wang, Q.F. An, H. Guo, Counterion exchanged hydrophobic polyelectrolyte multilayer membrane for organic solvent nanofiltration, J. Membr. Sci., 620 (2021) 118827.

[35] Z. Lai, Development of ZIF-8 membranes: Opportunities and challenges for commercial applications, Curr. Opin. Chem. Eng., 20 (2018) 78-85.

[36] Z. Wang, Z. Si, D. Cai, G.L. Shufeng Li, P. Qin, Synthesis of stable COF-300 nanofiltration membrane via in-situ growth with ultrahigh flux for selective dye separation, J. Membr. Sci., 615 (2020) 118466.

[37] Z. Zhai, N. Zhao, W. Dong, P. Li, H. Sun, Q.J. Niu, In situ assembly of a zeolite imidazolate framework hybrid thin-film nanocomposite membrane with enhanced desalination performance induced by noria-polyethyleneimine codeposition, ACS Appl. Mater. Interfaces, 11 (2019) 12871-12879.

[38] X.-p. Wang, J. Hou, F.-s. Chen, X.-m. Meng, In-situ growth of metal-organic framework film on a polydopamine-modified flexible substrate for antibacterial and forward osmosis membranes, Sep. Purif. Technol., 236 (2020) 116239.

[39] J. Campbell, G. Székely, R.P. Davies, D.C. Braddock, A.G. Livingston, Fabrication of hybrid polymer/metal organic framework membranes: Mixed matrix membranes versus in situ growth, J. Mater. Chem. A, 2 (2014) 9260-9271.

[40] X. Wu, L. Yang, F. Meng, W. Shao, X. Liu, M. Li, ZIF-8-incorporated thin-film nanocomposite (TFN) nanofiltration membranes: Importance of particle deposition methods on structure and performance, J. Membr. Sci., 632 (2021) 119356.

[41] C. Van Goethem, R. Verbeke, M. Pfanmöller, T. Koschine, M. Dickmann, T. Timpel-Lindner, W. Egger, S. Bals, I.F.J. Vankelecom, The role of MOFs in thin-film nanocomposite (TFN) membranes, J. Membr. Sci., 563 (2018) 938-948.

[42] S. Yang, Y. Wang, P. Lu, H. Jin, F. Pan, Z. Shi, X.-s. Jiang, C. Chen, Z. Jiang, Y. Li, Metal–organic frameworks corset with a thermosetting polymer for improved molecular-sieving property of mixed-matrix membranes, ACS Appl. Mater. Interfaces, 12 (2020) 55308-55315.

[43] Y. Wei, Y. Wang, L. Wang, H. Yang, H. Jin, P. Lu, Y. Li, Simultaneous phase-inversion and crosslinking in organic coagulation bath to prepare organic solvent forward osmosis membranes, J. Membr. Sci., 620 (2021) 118829.

[44] K. Vanherck, G. Koeckelberghs, I.F.J. Vankelecom, Crosslinking polyimides for membrane applications: A review, Prog. Polym. Sci., 38 (2013) 874-896.

[45] S. Yang, H. Li, X. Zhang, S. Du, J. Zhang, B. Su, X. Gao, B. Mandal, Amine-functionalized ZIF-8 nanoparticles as interlayer for the improvement of the separation performance of organic solvent nanofiltration (OSN) membrane, J. Membr. Sci., (2020) 118433.

[46] M. Wu, H. Ye, F. Zhao, B. Zeng, High-quality metal–organic framework ZIF-8 membrane supported on electrodeposited ZnO/2-methylimidazole nanocomposite: Efficient adsorbent for the enrichment of acidic drugs, Sci. Rep., 7 (2017) 39778.

[47] S. Park, H.K. Jeong, In-situ linker doping as an effective means to tune zeolitic-imidazolate framework-8 (ZIF-8) fillers in mixed-matrix membranes for propylene/propane separation, J. Membr. Sci., 596 (2020) 117689.

[48] Y. Fan, H. Yu, S. Xu, Q. Shen, H. Ye, N. Li, Zn(II)-modified imidazole containing polyimide/ZIF-8 mixed matrix membranes for gas separations, J. Membr. Sci., 597 (2020) 117775.

[49] S.-J. Park, S.J. Kwon, H.-E. Kwon, M.G. Shin, S.-H. Park, H. Park, Y.-I. Park, S.-E. Nam, J.-H. Lee, Aromatic solvent-assisted interfacial polymerization to prepare high performance thin film composite reverse osmosis membranes based on hydrophilic supports, Polymer, 144 (2018) 159-167.

[50] S. Zhang, F. Fu, T.-S. Chung, Substrate modifications and alcohol treatment on thin film composite membranes for osmotic power, Chem. Eng. Sci., 87 (2013) 40-50.

[51] R.W. Baker, Membrane transport theory, Third Ed., Wiley, New York, 2012.

[52] W. Morris, C.J. Stevens, R.E. Taylor, C. Dybowski, O.M. Yaghi, M.A. Garcia-Garibay, NMR and X-ray study revealing the rigidity of zeolitic imidazolate frameworks, The J. Phys. Chem. C, 116 (2012) 13307-13312.

[53] Y. Li, J. Li, R.B. Soria, A. Volodine, B. Van der Bruggen, Aramid nanofiber and

modified ZIF-8 constructed porous nanocomposite membrane for organic solvent nanofiltration, J. Membr. Sci., 603 (2020) 118002.

[54] M.F.J. Solomon, Y. Bhole, A.G. Livingston, High flux membranes for organic solvent nanofiltration (OSN)-interfacial polymerization with solvent activation, J. Membr. Sci., 423 (2012) 371-382.

[55] K. Vanherck, A. Cano-Odena, G. Koeckelberghs, T. Dedroog, I. Vankelecom, A simplified diamine crosslinking method for PI nanofiltration membranes, J. Membr. Sci., 353 (2010) 135-143.

[56] Y. Li, L.H. Wee, J.A. Martens, I.F.J. Vankelecom, Interfacial synthesis of ZIF-8 membranes with improved nanofiltration performance, J. Membr. Sci., 523 (2017) 561-566.

[57] H.T. Kwon, H.-K. Jeong, A.S. Lee, H.S. An, J.S. Lee, Heteroepitaxially grown zeolitic imidazolate framework membranes with unprecedented propylene/propane separation performances, J. Am. Chem. Soc., 137 (2015) 12304-12311.

[58] M. Taheri, D. Ashok, T. Sen, T.G. Enge, N.K. Verma, A. Tricoli, A. Lowe, D. R. Nisbet, T. Tsuzuki, Stability of ZIF-8 nanopowders in bacterial culture media and its implication for antibacterial properties, Chem. Eng. J., (2020) 127511.

[59] X. Qiao, T.-S. Chung, Diamine modification of P84 polyimide membranes for pervaporation dehydration of isopropanol, AIChE J., 52 (2006) 3462-3472.

[60] D. Hua, Y.K. Ong, Y. Wang, T. Yang, T.-S. Chung, ZIF-90/P84 mixed matrix membranes for pervaporation dehydration of isopropanol, J. Membr. Sci., 453 (2014) 155-167.

[61] J. Campbell, J.D.S. Burgal, G. Szekely, R.P. Davies, D.C. Braddock, A. Livingston, Hybrid polymer/MOF membranes for organic solvent nanofiltration (OSN): Chemical modification and the quest for perfection, J. Membr. Sci., 503 (2016) 166-176.

[62] Y. Li, L.H. Wee, A. Volodin, J.A. Martens, I.F.J. Vankelecom, Polymer supported ZIF-8 membranes prepared via an interfacial synthesis method, Chem. Commun., 51 (2015) 918-920.

[63] R. Zhang, S. Ji, N. Wang, L. Wang, G. Zhang, J.-R. Li, Coordination-driven in situ self-assembly strategy for the preparation of metal–organic framework hybrid membranes, Angew Chem Int Ed Engl, 53 (2014) 9775-9779.

[64] H. Siddique, Y. Bhole, L.G. Peeva, A.G. Livingston, Pore preserving crosslinkers for polyimide OSN membranes, J. Membr. Sci., 465 (2014) 138-150.

[65] H. Lu, S. Zhu, Interfacial synthesis of free-standing metal–organic framework membranes, Eur. J. Inorg. Chem., 2013 (2013) 1294-1300.

[66] S. Japip, K.-S. Liao, Y. Xiao, T.-S. Chung, Enhancement of molecular-sieving properties by constructing surface nano-metric layer via vapor cross-linking, J. Membr. Sci., 497 (2016) 248-258.

[67] M.D.R. Weber, T.L. Baker, B. Dao, C. Kwon, F. Tian, Exploring the aggregative growth of nanoporous zeolitic imidazolate framework ZIF-8, Cryst. Growth Des., 20 (2020) 2305-2312.

[68] D. Saliba, M. Ammar, M. Rammal, M. Al-Ghoul, M. Hmadeh, Crystal growth of ZIF-8, ZIF-67, and their mixed-metal derivatives, J. Am. Chem. Soc., 140 (2018) 1812-1823.

[69] T.H. Lee, J.Y. Oh, S.P. Hong, J.M. Lee, S.M. Roh, S.H. Kim, H.B. Park, ZIF-8 particle size effects on reverse osmosis performance of polyamide thin-film nanocomposite membranes: Importance of particle deposition, J. Membr. Sci., 570-571 (2019) 23-33.

[70] I.H. Aljundi, Desalination characteristics of TFN-RO membrane incorporated with ZIF-8 nanoparticles, Desalination., 420 (2017) 12-20.

[71] J. Duan, Y. Pan, F. Pacheco, E. Litwiller, Z. Lai, I. Pinnau, High-performance polyamide thin-film-nanocomposite reverse osmosis membranes containing hydrophobic zeolitic imidazolate framework-8, J. Membr. Sci., 476 (2015) 303-310.

[72] X.-H. Ma, Z.-K. Yao, Z. Yang, H. Guo, Z.-L. Xu, C.Y. Tang, M. Elimelech, Nanofoaming of polyamide desalination membranes to tune permeability and selectivity, Environ. Sci. Technol. Lett., 5 (2018) 123-130.

[73] L.E. Peng, Z. Yao, Z. Yang, H. Guo, C.Y. Tang, Dissecting the role of substrate on the morphology and separation properties of thin film composite polyamide membranes: Seeing is believing, Environ. Sci. Technol., 54 (2020) 6978-6986.

[74] J.-A.-D. Sharabati, S. Guclu, S. Erkoc-Ilter, D.Y. Koseoglu-Imer, S. Unal, Y.Z. Menceloglu, I. Ozturk, I. Koyuncu, Interfacially polymerized thin-film composite membranes: Impact of support layer pore size on active layer polymerization and seawater desalination performance, Sep. Purif. Technol., 212 (2019) 438-448.

[75] X. Wu, L. Yang, F. Meng, W. Shao, X. Liu, M. Li, ZIF-8-incorporated thin-film nanocomposite (TFN) nanofiltration membranes: Importance of particle deposition methods on structure and performance, J. Membr. Sci., 632 (2021) 119356.

[76] L. Xu, J. Xu, B. Shan, X. Wang, C. Gao, Novel thin-film composite membranes via manipulating the synergistic interaction of dopamine and m-phenylenediamine for highly efficient forward osmosis desalination, J. Mater. Chem. A, 5 (2017) 7920-7932.

[77] M. Shan, H. Kang, Z. Xu, N. Li, M. Jing, Y. Hu, K. Teng, X. Qian, J. Shi, L. Liu, Decreased cross-linking in interfacial polymerization and heteromorphic support between nanoparticles: Towards high-water and low-solute flux of hybrid forward osmosis membrane, J. Colloid Interf. Sci, 548 (2019) 170-183.

[78] F. Xiao, B. Wang, X. Hu, S. Nair, Y. Chen, Thin film nanocomposite membrane containing zeolitic imidazolate framework-8 via interfacial polymerization for highly permeable nanofiltration, J. Taiwan Inst. Chem. Eng., 83 (2018) 159-167.

[79] J.H. Kim, S.J. Moon, S.H. Park, M. Cook, A.G. Livingston, Y.M. Lee, A robust thin film composite membrane incorporating thermally rearranged polymer support for organic solvent nanofiltration and pressure retarded osmosis, J. Membr. Sci., 550 (2018) 322-331.

[80] Z.F. Gao, G.M. Shi, Y. Cui, T.-S. Chung, Organic solvent nanofiltration (OSN) membranes made from plasma grafting of polyethylene glycol on cross-linked polyimide ultrafiltration substrates, J. Membr. Sci., 565 (2018) 169-178.

[81] M. Razali, C. Didaskalou, J.F. Kim, M. Babaei, E. Drioli, Y.M. Lee, G. Szekely, Exploring and exploiting the effect of solvent treatment in membrane separations, ACS Appl. Mater. Interfaces, 9 (2017) 11279-11289.

[82] S. Hermans, H. Mariën, C. Van Goethem, I.F.J. Vankelecom, Recent developments in thin film (nano)composite membranes for solvent resistant nanofiltration, Curr. Opin. Chem. Eng., 8 (2015) 45-54.

[83] S. Hermans, E. Dom, H. Mariën, G. Koeckelberghs, I.F.J. Vankelecom, Efficient synthesis of interfacially polymerized membranes for solvent resistant nanofiltration, J. Membr. Sci., 476 (2015) 356-363.

[84] S. Sorribas, P. Gorgojo, C. Téllez, J. Coronas, A.G. Livingston, High flux thin film nanocomposite membranes based on metal–organic frameworks for organic solvent nanofiltration, J. Am. Chem. Soc., 135 (2013) 15201-15208.

[85] D. Ma, G. Han, Z.F. Gao, S.B. Chen, Continuous UiO-66-type metal–organic framework thin film on polymeric support for organic solvent nanofiltration, ACS Appl. Mater. Interfaces, 11 (2019) 45290-45300.

[86] Q. Liu, X. Wu, K. Zhang, Polysulfone/polyamide-SiO_2 composite membrane with high permeance for organic solvent nanofiltration, Membranes, 8 (2018) 89.

[87] D. Hua, T.-S. Chung, Polyelectrolyte functionalized lamellar graphene oxide membranes on polypropylene support for organic solvent nanofiltration, Carbon, 122 (2017) 604-613.

[88] L. Paseta, J.M. Luque-Alled, M. Malankowska, M. Navarro, P. Gorgojo, J. Coronas, C. Téllez, Functionalized graphene-based polyamide thin film nanocomposite membranes for organic solvent nanofiltration, Sep. Purif. Technol., 247 (2020) 116995.

[89] C. Li, S. Li, L. Tian, J. Zhang, B. Su, M.Z. Hu, Covalent organic frameworks (COFs)-incorporated thin film nanocomposite (TFN) membranes for high-flux organic solvent nanofiltration (OSN), J. Membr. Sci., 572 (2019) 520-531.

[90] Y. Xu, F. You, H. Sun, L. Shao, Realizing mussel-inspired polydopamine selective layer with strong solvent resistance in nanofiltration toward sustainable reclamation, ACS Sustainable Chem. Eng., 5 (2017) 5520-5528.

[91] S. Li, C. Li, X. Song, B. Su, B. Mandal, B. Prasad, X. Gao, C. Gao, Graphene quantum dots-doped thin film nanocomposite polyimide membranes with enhanced solvent resistance for solvent-resistant nanofiltration, ACS Appl. Mater. Interfaces, 11 (2019) 6527-6540.

[92] J. Dai, S. Li, J. Liu, J. He, J. Li, L. Wang, J. Lei, Fabrication and characterization of a defect-free mixed matrix membrane by facile mixing PPSU with ZIF-8 core–shell microspheres for solvent-resistant nanofiltration, J. Membr. Sci., 589 (2019) 117261.